



Physics-Informed Conditional Autoencoder Approach for Robust Metabolic CEST MRI at 7T

Junaid R. Rajput^{1,2(✉)}, Tim A. Möhle¹, Moritz S. Fabian¹,
Angelika Mennecke¹, Jochen A. Sembill³, Joji B. Kuramatsu³,
Manuel Schmidt¹, Arnd Dörfler¹, Andreas Maier², and Moritz Zaiss¹

¹ Institute of Neuroradiology, University Hospital Erlangen, Erlangen, Germany

² Pattern Recognition Lab Friedrich-Alexander-University Erlangen-Nürnberg,
Erlangen, Germany
junaid.rajput@fau.de

³ Department of Neurology, University Hospital Erlangen-Nürnberg, Erlangen,
Germany

Abstract. Chemical exchange saturation transfer (CEST) is an MRI method that provides insights on the metabolic level. Several metabolite effects appear in the CEST spectrum. These effects are isolated by Lorentzian curve fitting. The separation of CEST effects suffers from the inhomogeneity of the saturation field B_1 . This leads to inhomogeneities in the associated metabolic maps. Current B_1 correction methods require at least two sets of CEST-spectra. This at least doubles the acquisition time. In this study, we investigated the use of an unsupervised physics-informed conditional autoencoder (PICAe) to efficiently correct B_1 inhomogeneity and isolate metabolic maps while using a single CEST scan. The proposed approach integrates conventional Lorentzian model into the conditional autoencoder and performs voxel-wise B_1 correction and Lorentzian line fitting. The method provides clear interpretation of each step and is inherently generative. Thus, CEST-spectra and fitted metabolic maps can be created at arbitrary B_1 levels. This is important because the B_1 dispersion contains information about the exchange rates and concentration of metabolite protons, paving the way for their quantification. The isolated maps for tumor data showed a robust B_1 correction and more than 25% increase in structural similarity index (SSIM) with gadolinium reference image compared to the standard interpolation-based method and subsequent Lorentzian curve fitting. This efficient correction method directly results in at least 50% reduction in scan time.

Keywords: Physics-informed autoencoder · CEST · Bound loss · Lorentzian fit · Acquisition time · Interpretability

Supplementary Information The online version contains supplementary material available at https://doi.org/10.1007/978-3-031-43993-3_44.

© The Author(s), under exclusive license to Springer Nature Switzerland AG 2023
H. Greenspan et al. (Eds.): MICCAI 2023, LNCS 14227, pp. 449–458, 2023.
https://doi.org/10.1007/978-3-031-43993-3_44

1 Introduction

Chemical exchange saturation transfer (CEST) is a novel metabolic magnetic resonance imaging (MRI) method that allows to detect molecules in tissue based on chemical exchange of their mobile protons with water protons [18]. CEST works by selectively saturating the magnetization of a specific pool of protons, such as those in metabolites or proteins, by applying narrow-band radiofrequency (RF) pulses at their respective Larmor frequency. Due to chemical exchange this saturation state is transferred to the water pool and a decrease in the detected water signal provides information about the concentration and exchange rate of the underlying molecules. This procedure is repeated for several RF frequencies to acquire the so-called CEST-spectrum in each voxel. CEST-MRI offers several promising contrasts that correlate with the diagnosis of diseases such as ischemic stroke [16], brain tumors [1], and neurodegenerative diseases [2, 5]. The CEST-spectrum contains effects of proton pools of various chemical components in the tissue, typically isolated by a Lorentzian model [14] that is derived from the underlying physics of the Bloch-McConnell equations [8]. In this conventional method, several Lorentzian distributions are fitted to the CEST-spectrum using nonlinear least squares method [10], and the amplitude of each fitted distribution represents a particular metabolic map.

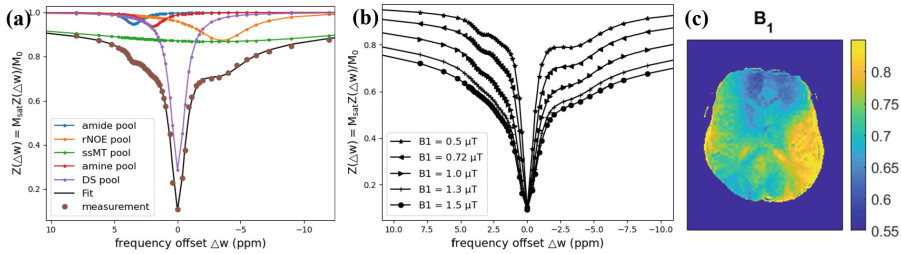


Fig. 1. (a) CEST-spectrum and the corresponding 5-pool Lorentzian fit. (b) CEST-spectrum dependence on B_1 saturation amplitude. (c) The B_1 inhomogeneity map at 7T.

The number of Lorentzian functions utilized in this process depends on the expected number of exchanging proton pools present in the spectrum. Figure 1a shows an example of an acquired CEST-spectrum and the corresponding 5-pool Lorentzian fit. Increasing the static magnetic field B_0 (e.g., with $B_0 = 7\text{T}$), enhances spectral resolution, but leads to significant variations in the B_1 amplitude of the saturating RF field across the field of view (cf. Fig. 1c). This B_1 inhomogeneity is corrected by acquiring CEST-spectra at various RF field strengths (cf. Fig. 1b) and then interpolating between them at fixed B_1 to produce the B_1 -robust metabolic CEST contrast maps [14]. This B_1 correction increases the acquisition time at least twofold.

Hunger et al. shown that supervised learning can be used to generate B_1 -robust CEST maps, coining the DeepCEST approach [3, 4]. However, the previous work on generating the B_1 -robust CEST contrasts rely on valid target data

and the underlying assumptions to generate it, and can only create CEST maps at one particular B_1 level.

In this work, we developed a conditional autoencoder (CAE) [13] to generate B_1 -homogeneous CEST-spectra at arbitrary B_1 levels, and a physics-informed autoencoder (PIAE) to fit the 5-pool Lorentzian model to the B_1 corrected CEST-spectra. This inclusion of physical knowledge in the form of known operators in neural nets (NN) is expected to reduce the absolute error margin of the model [6, 7] and to increase its interpretability. Both CAE and PIAE are trained in an unsupervised end-to-end method that eliminates the shortcomings of conventional Lorentzian curve fitting and produces robust CEST contrast at arbitrary B_1 levels without the need for an additional acquisition scan. We called the proposed method physics-informed conditional autoencoder (PICAE).

2 Methods

Data Measurements. CEST imaging was performed in seven subjects, including two glioblastoma patients, after written informed consent was obtained to investigate the dependence of CEST effects on B_1 in brain tissue. The local ethics committee approved the study. All volunteers were measured at three B_1 field strengths $0.72 \mu\text{T}$, $1.0 \mu\text{T}$, and $1.5 \mu\text{T}$. A method as described by Mennecke et al. [9] was used to acquire CEST data on a 7T whole-body MRI system (MAGNETOM Terra, Siemens Healthcare GmbH, Erlangen, Germany). Saturated images were obtained for 54 non-equidistant frequency offsets ranging from -100 ppm to $+100$ ppm. The acquisition time per B_1 level was 6:42 min. The acquisition of the B_1 map required an additional 1:06 min.

Conditional Autoencoder. We developed a conditional autoencoder (CAE) to solve the B_1 inhomogeneity problem, which is essential for the generation of metabolic CEST contrast maps at 7T. The left part of Fig. 2 describes the CAE. The encoding network of CAE took the raw CEST-spectrum and the corresponding effective B_1 value as input and generate a latent space that was concatenated once with the same B_1 input value and passed to the decoder that reconstruct the uncorrected B_1 CEST-spectrum, and another time the latent space was concatenated with the desired/specific effective B_1 value to reconstruct the CEST-spectrum at a specific B_1 saturation amplitude. Both decoders shared the weights (cf. Fig. 2). For the development of the CAE networks, we used the well-known fully concatenated (FC) layers with leaky ReLU activations except for the last layer of decoder, which had a linear activation. The encoder and decoder both consisted of 4 layers, where the layers of the encoder successively contain 128, 128, 64, 32 neurons, while the layers of the decoder successively contain 32, 64, 128, 128 neurons. The input, latent space and output layers had 55, 17 and 54 neurons respectively.

Physics-Informed Autoencoder. The Lorentzian model and its B_1 -dispersion can be derived from the underlying spin physics described by

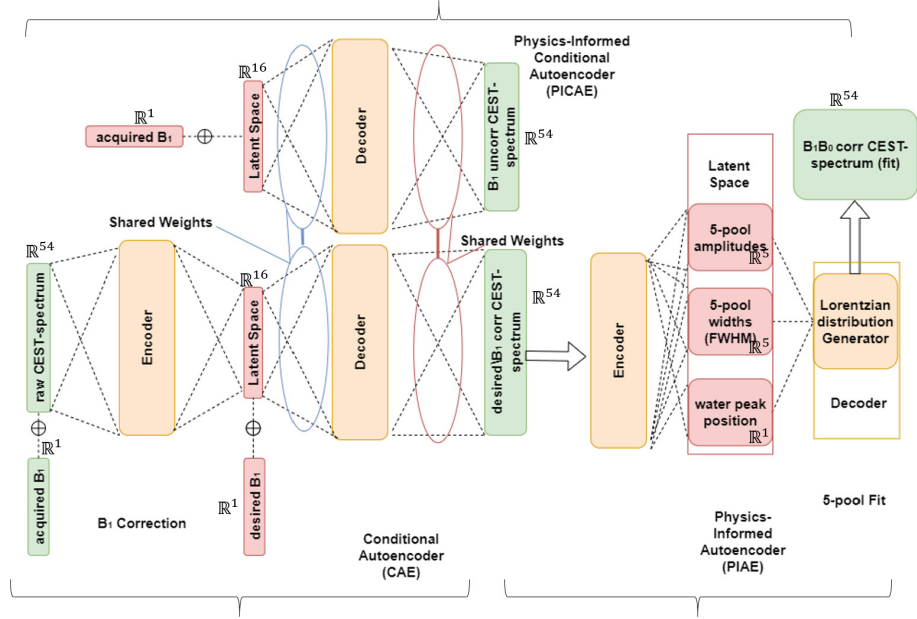


Fig. 2. Overview of the proposed physics-informed conditional autoencoder for B₁ inhomogeneity correction (left) and Lorentzian curve fitting (right).

the Bloch-McConnell equation system [8]. The physics-informed autoencoder (PIAE) utilized fully connected NN as encoder and Lorentzian distribution generator as a decoder to perform the pixel-wise 5-pool Lorentzian curve fit to the CEST-spectrum (water, amide, amine, NOE, MT) [14]. The 5-pool model was described as

$$Z(\Delta\omega) = 1 - L_{DS} - L_{ssMT} - L_{amine} - L_{rNOE} - L_{amide}, \quad (1)$$

where L denotes the Lorentz function. The direct saturation pool (water) was defined as

$$L_{DS} = \frac{A_{DS}}{1 + \left(\frac{\Delta\omega - \delta_{DS}}{\tau_{DS}/2}\right)^2}. \quad (2)$$

The remaining other four pools were defined as

$$L_i = \frac{A_i}{1 + \left(\frac{\Delta\omega - \delta_{DS} - \delta_i}{\tau_i/2}\right)^2}, \quad i \in amide, amine, rNOE, ssMT. \quad (3)$$

The right part of Fig. 2 describes the PIAE. The encoder of PIAE mapped the CEST-spectrum to the amplitudes A_i , the full width half maximum (FWHM) τ_i , and the water peak position δ_{DS} of the 5-pool Lorentzian model. Its encoder consisted of four FC layers, each with 128 neurons with leaky ReLU activations. It had three so-called FC latent space layers with linear activation for position

and exponential activations for FWHM and amplitudes of 5-pool Lorentzian model. The positions of amide, rNOE, ssMT, and amine were fixed at 3.5 ppm, -3.5 ppm, -3 ppm, and 2 ppm, respectively, and shifted with respect to the predicted position of the water peak. The decoder of PIAE consisted of a Lorentzian distribution generator (cf. Fig. 2). It generated samples of the 5-pool distributions exactly at the offsets $\Delta\omega$ (i.e. between -100 ppm and 100 ppm) where the input CEST-spectrum was sampled, and combined them according to Eq. 1 to generate the input CEST spectrum with or without B_0 correction.

Bound Loss. The peak positions δ_i and widths τ_i of the pools had to be within certain bounds so that certain neurons in the latent space layer of PIAE would not be exchanged and provide the same pool parameters for all samples. We developed a simple cost function along the lines of the hinge loss [12], called the bound loss. Mathematically, it is defined as follows

$$bound\ loss = \left\{ \begin{array}{ll} abs(y - lb), & \text{if } y < lb \\ abs(y - ub), & \text{if } y > ub \\ 0, & \text{if } y \leq ub \text{ AND } y \geq lb \end{array} \right\}. \quad (4)$$

The bound loss increases linearly as the output of the latent space neurons of PIAE exceeds or recede from the boundaries. The lower and upper limits for positions and widths are given in Table 1 of the supplementary material.

Training and Evaluation. Four healthy volunteers formed the training and validation sets. The test set consisted of the two tumor patients and one healthy subject. To ensure that the outcomes were exclusively based on the CEST-spectrum and not influenced by spatial position, the training was carried out voxel-by-voxel. Consequently, there were approximately one million CEST-spectra for the training process. CAE was first trained with MSE loss. In this step, the CAE encoder was fed with the CEST-spectrum of a specific B_1 saturation amplitude, and it generated two CEST-spectra, one for the input B_1 saturation level and the other for the B_1 level injected into the latent space (cf. Fig. 2). Later, it was trained with a combination of MSE loss and perception loss (MSE loss between the latent space of the CEST-spectra at two different B_1 levels). To incorporate perception loss, we used two forward passes with two different B_1 CEST-spectra and used perception loss to generate a latent space that is independent of B_1 saturation amplitude. The following equation describes the loss of the second step.

$$CAE\ loss = MSE\ loss + 0.1 \cdot perception\ loss \quad (5)$$

PIAE, on the other hand, was trained with a combination of MSE loss and bound loss. The PIAE loss was described as follows

$$PIAE\ loss = MSE\ loss + bound\ loss, \quad (6)$$

for evaluation we input the uncorrected CEST-spectrum acquired at $1\mu\text{T}$ and generated corrected CEST-spectra at B_1 0.5, 0.72, 1.0, 1.3, 1.5 μT . PIAE encoder yielded the amplitudes of 5-pool for B_1 corrected CEST-spectrum. Its decoder reconstructed the B_1B_0 fitted CEST-spectrum. The B_0 correction simply refers to the shift of the position of the water peak to 0 ppm.

CEST Quantification. The multi- B_1 CEST-spectra allow quantification of CEST effects (amide, rNOE, amine) [14,15] down to the exchange rate and concentration. The amplitudes of the CEST contrasts were expressed according to the definition in [15] as follows

$$A_i = \underbrace{f_i k_i}_{Z_1} \underbrace{\frac{w_1^2}{k_i(k_i + r_{2i}) + w_1^2}}_{\underbrace{Z_2}_{\alpha}} Z_{ref} \quad i \in \text{amide, amine, rNOE}, \quad (7)$$

where f_i , k_i , and r_{2i} express the concentrations, exchange rates, and relaxation rates of the pools. Z_{ref} defines the sum of all 5 distributions at the resonance frequency of the specific pool in B_1B_0 corrected CEST-spectrum and w_1 is the frequency of the oscillating field.

The amplitudes of CEST contrasts in the Lorentzian function have the B_1 dispersion function given by the labeling efficiency α (Eq. 7). The exchange rate occurs here separately from the concentration, which allows their quantification via the B_1 dispersion. Concentration and exchange rate were fitted as a product and denoted as Z_1 (quantified maps), and $k(k+r_2)$ was also fitted with the single term Z_2 using trust-region reflective least squares [10].

3 Results

The comparison of PICAIE with the conventional method [9,14] is shown in columns 1 and 2 of Fig. 3. The top image in column 3 shows the T_1 -weighted reference image enhanced with the exogenous contrast agent gadolinium (Gd- T_1w), and the bottom image shows the B_1 -map. The tumor shows a typical so called gadolinium ring enhancement indicated by the arrow (a_{15}), which is also visible in the non-invasive and gadolinium-free CEST contrast maps (columns 1 and 2). The PICAIE-CEST maps showed better visualization of this tumor feature compared to the conventional method. The proposed method yielded at least 25% increase in the structural similarity index (SSIM) with the Gd- T_1w image for the ring enhancement region. The contrast maps also appear less noisy and more homogeneous over the whole brain compared to the Lorentzian fit on the interpolated-corrected B_1 CEST-spectra [14]. To further evaluate the performance of PIAE and CAE, we b1-corrected the data using CAE and fitted it with the least squares method (CAE-Lorentzian fit). The comparison of the CEST maps produced by the conventional Lorentzian fit, the CAE-Lorentzian fit, and PICAIE is shown in Table 1 using SSIM and gradient cross correlation (GCC)

[11] for the Tumor ring region. Both the CAE-Lorentzian fit and PICAE were better than the conventional method. CAE-Lorentzian fit even outperformed PICAE for rNOE metabolic map and has similar performance for amide, but it has much lower performance for amine.

Table 1. Comparision of PICAE with conventional and CAE-Lorentzian fit. SSIM and GCC are calculated with respected to the Gd image for tumor region.

Fit method	amide		rNOE		amine	
	SSIM	GCC	SSIM	GCC	SSIM	GCC
Conventional Lorentzian fit	0.09	0.13	0.10	0.18	0.09	0.07
CAE-Lorentzian fit	0.11	0.14	0.18	0.3	0.10	0.18
PICAE	0.12	0.13	0.14	0.27	0.16	0.27

The ability of PICAE to produce B_1 -robust CEST maps at arbitrary levels is shown in Fig. 4, where different B_1 levels reveal different features of the heterogenous tumor. Quantification of chemical exchange rates and concentration, i.e., $Z_1 = f \cdot k$, is shown in column 4. Z_1 (quantified maps) further improve the visualization of the ring enhancement area. Column 5 shows the Z_2 maps, which are combination of the exchange rate k and the relaxation rate r_2 . Quantified maps of amide, rNOE and amine for another tumor patient is shown in supplementary Fig. 1. The accuracy of the CAE to generate particular B_1 CEST-spectra is depicted using absolute error for acquisition at different B_1 levels (see supplementary Fig. 2). The performance was lower for B_1 0.72 μ T, and 1.5 μ T compared to 1 μ T.

4 Discussion

In this work, we analyzed the use of an autoencoder approach to generate B_1 -robust CEST contrast maps at arbitrary B_1 levels, which requires multiple acquisitions in conventional methods [14]. The proposed method reduces the acquisition time by at least half when only two acquisitions are performed for B_1 correction. Supervised learning (DeepCEST) can generate CEST maps that are not susceptible to B_1 inhomogeneity at a particular B_1 , which already reduces acquisition time. However, DeepCEST was trained on data fitted using a conventional pipeline [9, 14] which has suboptimal B_1 correction (cf. Fig. 3). Moreover, the different pools in the CEST spectrum are highlighted at different B_1 levels (cf. Fig. 4). An approach that can generate a B_1 -robust CEST-spectrum at multiple B_1 levels allows quantifying the exchange rate and concentration of the CEST pools [15]. The optimal B_1 can often only be selected at post-processing during the analysis of clinical data, as some clinically important features appear better at certain B_1 levels (cf. Fig. 4). The proposed PICAE approach combines B_1 correction and Lorentzian curve fitting in a single step. The B_1 correction

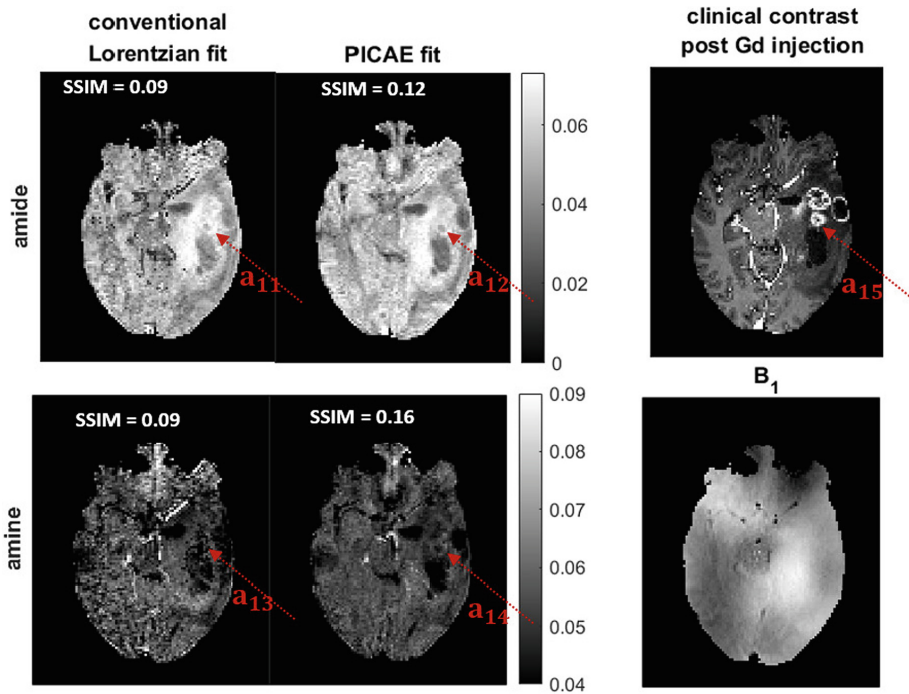


Fig. 3. Comparison of B_1 corrected CEST maps for conventional and PICA methods (Columns 1 and 2). The top image in column 3 shows a reference Gd- T_1 w image, while the bottom image shows the B_1 map. SSIM are calculated with respect to the Gd image for tumor region.

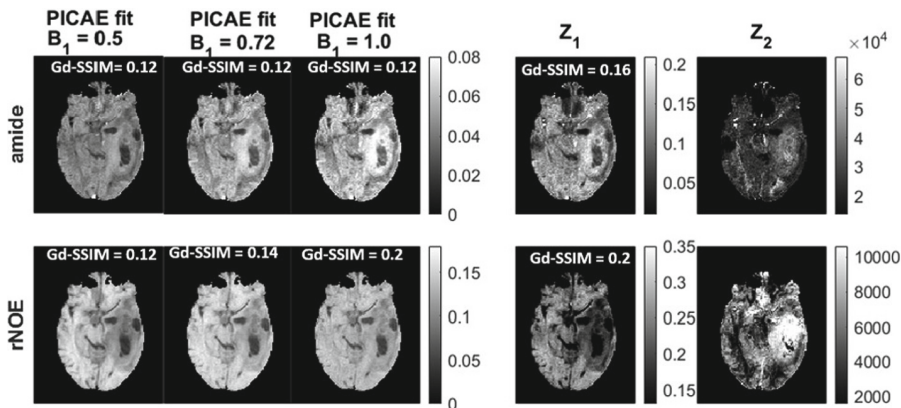


Fig. 4. B_1 -robust CEST maps at 0.5, 0.72, and 1.0 μ T (columns 1–3), quantified maps (column 4), and combination of exchange and relaxation rates (column 5). SSIM are calculated with respect to the Gd image for tumor region.

was performed with a CAE, while the Lorentzian line fitting was performed with a PIAE using NN as the encoder and Lorentzian distribution generator as the decoder. This allows interpretation of the model while overcoming the drawback of curve fitting, such as being prone to noise (cf. Fig. 3).

The bound loss ensured that the positions of the pools were not interchanged. Quantification was still performed using the nonlinear least squares fit according to Eq. 7. The main reason for this was that it does not affect the acquisition time and it is affected by the Z_{ref} . The training was performed voxel-wise to ensure that the results are based only on the CEST-spectrum. This also results in about 1 million CEST-spectra for the training. Figure 3 shows the superiority of PICAE over the standard method, and Fig. 4 shows that the results produced by PICAE are authentic because the quantification column Z_1 matches the amplitude images and follows Eq. 7. CAE-Lorentzian fitting showed comparable performance for amide and rNOE maps, but significantly lower performance for amine because it was still fitted using the least squares method, which is susceptible to noise in the input and takes up to 5 min to evaluate, compared to PICAE, which takes only a few seconds. The 1 μ T acquisition performs better than 0.72 μ T and 1.5 μ T because it was trained for both lower and higher B_1 values compared to the other two acquisitions. The robustness of method for cyclic consistency [17] is displayed in supplementary Fig. 2, which also shows the interpretability of the method. The results of Fig. 3 and Fig. 4 also show the generalization capability of PICAE as it was trained without the tumor data.

5 Conclusion

In this work, we propose a PICAE method for evaluating 7T-CEST MRI that accounts for B_1 inhomogeneity in the input and predicts homogeneous metabolic CEST contrasts at arbitrary B_1 levels. The proposed generative and interpretable method enables (i) a reduction of scan time by at least 50%, (ii) the generation of reliable 7T-CEST contrast maps robust to B_1 inhomogeneity at multiple B_1 levels, (iii) a clear physical interpretation of the B_1 correction of the CEST-spectra and the fitting of the Lorentzian model to it, and (iv) the quantification of the CEST contrast maps.

References

1. Chen, L.Q., Pagel, M.D.: Evaluating pH in the extracellular tumor microenvironment using CEST MRI and other imaging methods. *Adv. Radiol.* **2015**, 25 (2015)
2. Dou, W., et al.: Chemical exchange saturation transfer magnetic resonance imaging and its main and potential applications in pre-clinical and clinical studies. *Quant. Imaging Med. Surg.* **9**(10), 1747–1766 (2019)
3. Glang, F., et al.: Linear projection-based CEST parameter estimation. *NMR Biomed.* (2022). <https://doi.org/10.1002/nbm.4697>
4. Hunger, L., et al.: Deepcest 7 t: fast and homogeneous mapping of 7 t CEST MRI parameters and their uncertainty quantification. *Magn. Reson. Med.* **89**, 1543–1556 (2023)

5. Lewerenz, J., Maher, P.: Chronic glutamate toxicity in neurodegenerative diseases—what is the evidence? *Front. Neurosci.* **9**, 469 (2015)
6. Maier, A.K., Schebesch, F., Syben, C., Würfl, T., Steidl, S., Choi, J.H., Fahrig, R.: Precision learning: Towards use of known operators in neural networks. In: 2018 24th International Conference on Pattern Recognition (ICPR), pp. 183–188 (2017)
7. Maier, A.K., et al.: Learning with known operators reduces maximum error bounds. *Nat. Mach. Intell.* **1**, 373–380 (2019)
8. McConnell, H.M.: Reaction rates by nuclear magnetic resonance. *J. Chem. Phys.* **28**, 430–431 (1958)
9. Mennecke, A., et al.: 7 tricks for 7 t CEST: improving reproducibility of multi-pool evaluation provides insights into effects of age and early stage parkinson’s disease. *NMR Biomed.* **36**(6), e4717 (2022)
10. Moré, J.J., Sorensen, D.C.: Computing a trust region step. *Siam J. Sci. Stat. Comput.* **4**, 553–572 (1983)
11. Penney, G.P., Weese, J., Little, J.A., Desmedt, P., Hill, D.L.G., Hawkes, D.J.: A comparison of similarity measures for use in 2d–3d medical image registration. In: International Conference on Medical Image Computing and Computer-Assisted Intervention (1998)
12. Rosasco, L., de Vito, E., Caponnetto, A., Piana, M., Verri, A.: Are loss functions all the same? *Neural Comput.* **16**, 1063–1076 (2004)
13. Sohn, K., Lee, H., Yan, X.: Learning structured output representation using deep conditional generative models. In: NIPS (2015)
14. Windschuh, J., et al.: Correction of b1-inhomogeneities for relaxation-compensated CEST imaging at 7 t. *NMR in Biomed.* **28**, 529–537 (2015)
15. Zaiss, M., Jin, T., Kim, S.G., Gochberg, D.F.: Theory of chemical exchange saturation transfer MRI in the context of different magnetic fields. *NMR Biomed.* **35**, e4789 (2022)
16. Zhou, J., Payen, J.F., Wilson, D.A., Traystman, R.J., van Zijl, P.C.M.: Using the amide proton signals of intracellular proteins and peptides to detect PH effects in MRI. *Nature Med.* **9**, 1085–1090 (2003)
17. Zhu, J.Y., Park, T., Isola, P., Efros, A.A.: Unpaired image-to-image translation using cycle-consistent adversarial networks. In: 2017 IEEE International Conference on Computer Vision (ICCV), pp. 2242–2251 (2017)
18. van Zijl, P.C.M., Yadav, N.N.: Chemical exchange saturation transfer (CEST): what is in a name and what isn’t? *Magn. Reson. Med.* **65**, 927–948 (2011)